Supporting Information

Elucidating the Proton-Coupled Oxygen Reduction Pathway in Protonic Ceramic Fuel Cells

Seulchan Kim[1†], Dogeun Yoon[1,2†], Jinwoong Chae[3], Hyeonwoo Kim[1,4], Jongsup Hong[2], Ji-Won Son[1,5], Jong-Ho Lee[1,6], Sungwoo Kang[3,6], and Ho-Il Ji[1,6*]

[1] *Hydrogen Energy Materials Research Center, Korea Institute of Science and Technology (KIST), Seoul 02792, Republic of Korea*

[2] *School of Mechanical Engineering, Yonsei University, Seoul 03722, Republic of Korea*

[3] *Computational Science Research Center, Korea Institute of Science and Technology (KIST), Seoul 02792, Republic of Korea*

[4] *Department of Materials Science and Engineering, Korea University, Seoul 02841, Republic of Korea*

[5] *Graduate school of Energy and Environment (KU-KIST Green School), Korea University, Seoul 02841, Republic of Korea*

[6] *Nanomaterials Science and Engineering, Korea University of Science and Technology (UST), KIST Campus, Seoul 02792, Republic of Korea*

† Equally contributed author

*Corresponding author.

E-mail address: hiji@kist.re.kr (H.-I. Ji)

Supplementary Note 1: Degree of hydration of BCFZY

To evaluate the degree of hydration (α) and hydrogenation $(1-\alpha)$ reactions in BCFZY, both thermogravimetric analysis (TGA) and electrical conductivity measurements were performed.

The value of α was calculated using Eq. (S1):

$$\Delta w_{H2O} = n_{TCO}\left(\alpha\frac{M_{H2O}}{2} + (1-\alpha)\frac{M_{H2}}{2}\right)[OH_O^{\circ}] \quad \text{(S1)}$$

where Δw_{H2O} is the mass change of the BCFZY sample upon water uptake, n_{TCO} is the mole number of the material, M_{H2O} and M_{H2} are the molar weights of H_2O (18.015 g mol^{-1}) and H_2 (2.016 g mol^{-1}), respectively, $[OH_O^{\circ}]$ represents the proton concentration incorporated into the oxide lattice.

In this calculation, α denotes the fractional contribution of the hydration reaction, whereas ($1-\alpha$) corresponds to the hydrogenation contribution. This equation can be correlated with the electrical conductivity expression and thus rearranged as follows:

$$\sigma_{H_2O} = e[h^{\circ}]_{H_2O}\mu_{h^{\circ}} = e([h^{\circ}]_{dry} - (1-\alpha)[OH_O^{\circ}])\mu_{h^{\circ}} \quad \text{(S2)}$$

$$\sigma_{H_2O} = e\left([h^{\circ}]_{dry} - (1-\alpha)\frac{2\Delta w_{H_2O}}{n_{TCO}(\alpha M_{H_2O} + (1-\alpha)M_{H2})}\right)\mu_{h^{\circ}} \quad \text{(S3)}$$

$$\sigma_{dry} - \sigma_{H_2O} = e\left((1-\alpha)\frac{2\Delta w_{H_2O}}{n_{TCO}(\alpha M_{H_2O} + (1-\alpha)M_{H2})}\right)\mu_{h^{\circ}} \quad \text{(S4)}$$

where σ_{dry} and σ_{H_2O} are the electrical conductivities under dry and humidified atmospheres, respectively; e is the elementary charge, $\mu_{h^{\circ}}$ is the hole mobility, and $[h^{\circ}]_{H_2O}$ and $[h^{\circ}]_{dry}$ denote the hole concentrations under humidified and dry conditions, respectively, at identical temperature and pO$_2$.

For the calculation of the above equation, the hole mobility ($\mu_{h^{\circ}}$) was also required. The hole mobility was determined from the difference in electrical conductivity ($\sigma_{\mathrm{I}} - \sigma_{\mathrm{II}}$) and hole concentration ($[h^{\circ}]_{\mathrm{I}} - [h^{\circ}]_{\mathrm{II}}$) at two oxygen partial pressures (pO$_2$,I and pO$_2$,II), as described by the following equation:

$$\begin{aligned}\sigma_{\mathrm{I}} - \sigma_{\mathrm{II}} &= e\left([h^{\circ}]_{\mathrm{I}} - [h^{\circ}]_{\mathrm{II}}\right)\mu_{h^{\circ}} \\ &\approx 2e\left([V_O^{\circ\circ}]_{\mathrm{II}} - [V_O^{\circ\circ}]_{\mathrm{I}}\right)\mu_{h^{\circ}}\end{aligned} \quad \text{(S5)}$$

In this analysis, the hole mobility was assumed to be independent of pO_2 and pH_2O at a given temperature. This approximation arises from the redox reaction ($\frac{1}{2}O_2 + V_O^{\circ\circ} \leftrightarrow O_O^x + 2h^\circ$) and the charge neutrality condition ($2[V_O^{\circ\circ}] + [h^\circ]$ = constant), which together indicate that the changes in hole concentration ($[h^\circ]_I - [h^\circ]_{II}$) are compensated by the changes in oxygen vacancy concentration ($[V_O^{\circ\circ}]_{II} - [V_O^{\circ\circ}]_I$) under different oxygen partial pressures.

The change in oxygen vacancy concentration between pO_2 = 0.21 atm and 0.10 atm at 550 °C was taken from literature, with a reported value of approximately 0.009 mol per mol of oxide. [1] Based on the change in electrical conductivity between pO_2 = 0.156 atm and 0.123 atm at 550 °C, the oxygen partial pressure dependence coefficient ($n = 0.236$) was determined according to Eq. (S7).

$$\sigma \propto [h^\circ] \propto pO_2^n \cdot pH_2O^m \quad \text{(S7)}$$

Using this coefficient, the conductivities at pO_2 = 0.21 and 0.10 atm were estimated, yielding a value of $\sigma_I - \sigma_{II}$ = 0.371 S cm^{-1}. Consequently, the hole mobility (μ_{h°) obtained from (Eq. S5) was 8.85 × 10^{-3} cm^2 V^{-1} s^{-1}.

For the calculation of Eq. S4, the mass change (Δw_{H_2O}) of the BCFZY sample was measured by TGA at 550 °C under dry air and 1.5 % H_2O-humidified air. The BCFZY pellet used for the TGA experiment was prepared following the same procedure as that described for the ECR measurements in the main text, with dimensions of 1.7 × 1.7 × 11.6 mm^3 and a mass of 0.186g. Using this sample (n_{TCO} = 7.6 × 10^{-4} mol), the measured mass change associated with water uptake (Δw_{H_2O}) was determined from the difference between the equilibrium masses under dry and humidified conditions, yielding a value of 8.0 × 10^{-6} g.

The variation in electrical conductivity between dry and 3% H_2O-humidified atmosphere at 550 °C was used to determine the H_2O partial pressure dependence coefficient (m = 1.27 x 10^{-3}) according to Eq. (S7). With this coefficient, the conductivity under 1.5% H_2O-humidified condition was subsequently estimated, giving a conductivity difference of ($\sigma_{dry} - \sigma_{H_2O}$) = 0.0137 S cm^{-1}.

Consequently, the value of α calculated from Eq. (S4) was approximately 0.84±0.01, indicating that, at 550 °C, about 84% of the water uptake in BCFZY occurs via the hydration reaction, while the remaining 16% proceeds through the hydrogenation reaction.

As discussed in Supplementary Note 6, the actual operating conditions of the cell involve local variations in pO_2 and pH_2O, as well as shifts in effective partial pressures induced by overpotential. Consequently, the thermodynamic environment significantly differs from the static partial pressure conditions employed for the mechanism study. To elucidate these shifts

in point defect equilibria, Merkle et al. systematically presented the variations in hole, oxygen vacancy, and proton concentrations as functions of pO_2 and pH_2O via thermodynamic calculations.[2] Their work serves as a crucial baseline for interpreting the results of this study.

The observed contribution of the hydrogenation reaction in this study is approximately 16%, suggesting that the regimes dominated by hydration and hydrogenation are not distinctively separated; rather, these two reaction mechanisms coexist and overlap within a certain range. Under these conditions, applying a fuel cell mode (FC bias) shifts the effective pO_2 to lower values and the effective pH_2O to higher values. Consequently, the system is likely to transition toward a regime where the hydration reaction becomes relatively more dominant, leading to an expected increase in the overall degree of hydration.

Conversely, under electrolysis mode (EC bias), the conditions shift toward higher effective pO_2 and lower effective pH_2O. This change is expected to reduce the relative contribution of the hydration reaction, thereby decreasing the overall degree of hydration.

Supplementary Note 2: Partial pressure dependence of defects between bulk and surface

At equilibrium, the electrochemical potential of species i is identical in the bulk (∞) and surface layer (s). Therefore, the following relationship can be derived:

$$\mu_i^s - \mu_i^\infty = -z_i F(\phi^s - \phi^\infty) \tag{S8}$$

where μ_i^s, μ_i^∞ denote the chemical potentials of species i at the surface and in the bulk, respectively, and ϕ represents the electrical potential.

By substituting the chemical potential term in Eq. (S8) with its activity expression ($\mu_i = \mu_i^0 + RT \ln a_i$) and differentiating with respect to ln $p\mathrm{O}_2$, the following relation is obtained:

$$RT\left(\frac{\partial \ln a_{i,s}}{\partial \ln p\mathrm{O}_2} - \frac{\partial \ln a_{i,\infty}}{\partial \ln p\mathrm{O}_2}\right) = -z_i F \frac{\partial(\phi^s - \phi^\infty)}{\partial \ln p\mathrm{O}_2} \tag{S9}$$

This indicates that the key factor is how the electrical potential difference between the surface and bulk ($\Delta\phi$)varies with $p\mathrm{O}_2$. In highly doped systems, the Debye length is relatively short, and for redox-active materials, the high electronic or ionic conductivity of charge carriers allows rapid compensation of local charge imbalance, resulting in a small $\Delta\phi$. Therefore, cathode materials used in PCFCs—being both highly doped and redox-active—are expected to exhibit essentially identical $p\mathrm{O}_2$ dependencies in the bulk and at the surface.

Supplementary Note 3: Partial pressure dependence of defects between bulk and surface

The experimentally determined pO_2 and pH_2O dependences of the reaction rate for R1 of PBSCF are summarized below.

$$\overset{\vee}{\Re}(\mathrm{R1}) \propto pO_2^{\,0.24\pm0.03} \cdot pH_2O^{\,0.00\pm0.01}$$

The objective is to identify the combination of exponents α (= 0, 1/2, 1), β (= 0, 1, 2), γ (= 0, −1, −2, −3), and ω (= 0, 1, 2) in the global rate expression of the RDS ($\overset{\vee}{\Re} \propto pO_2^{\,\alpha}[V_O^{\bullet\bullet}]^{\beta}[h^{\bullet}]^{\gamma}[OH_O^{\bullet}]^{\omega}$; Eq. 4) that best reproduces the observed pO_2 and pH_2O dependences. For this, the pO_2 and pH_2O dependences of the point-defect concentrations, as given in Eq. 6 of the main text, must be used.

$$[h^{\bullet}] \propto pO_2^{\,0.076} \cdot pH_2O^{0}$$

$$[V_O^{\bullet\bullet}] \propto pO_2^{\,-0.35} \cdot pH_2O^{0}$$

$$[OH_O^{\bullet}] \propto pO_2^{\,-0.174} \cdot pH_2O^{0.5}$$

Because the experimentally obtained $\overset{\vee}{\Re}(\mathrm{R1})$ shows no dependence on pH_2O, the exponent of the proton concentration, ω, can be set to 0. The remaining task is then to determine α, β, and γ such that the calculated pO_2 dependence matches the experimental value of 0.24 ± 0.03. Considering all possible combinations of α (= 0, 1/2, 1), β (= 0, 1, 2), and γ (= 0, −1, −2, −3), there are 36 candidates in total. Among them, only the following three combinations (α, β, γ) yield a pO_2 dependence consistent with 0.24 ± 0.03:

R1 in PBSCF	$\overset{\vee}{\Re} \propto pO_2^{\,\alpha}[V_O^{\bullet\bullet}]^{\beta}[h^{\bullet}]^{\gamma}[OH_O^{\bullet}]^{\omega}$				$\overset{\vee}{\Re} \propto pO_2^{\,A} \cdot pH_2O^{\,B}$	
	α	β	γ	ω	A	B
Case I	1	2	-1	0	0.224	0
Case II	1	2	0	0	0.300	0
Case III	1/2	0	-3	0	0.272	0

Based on these α, β, and γ values, the corresponding reactant combinations for the RDS are derived by referring to Tables 1–4. For example, in Case I, α = 1 requires that oxygen participates as diatomic O_2, β = 2 indicates that two oxygen vacancies participate as reactants, and γ = −1 requires that the reactants include a net negative charge of −1. Accordingly, the possible reactant sets are: (1) $O_{2,ad}^{-} + 2V_O^{\bullet\bullet}$ or (2) $(O_2^{-}\ \text{in}\ V_O^{\bullet\bullet}) + V_O^{\bullet\bullet}$.

For Case III, α = 1/2 implies that oxygen must participate in an atomic form, β = 0 means that oxygen vacancies do not participate as reactants, and γ = −3 requires that the reactants include

a net negative charge of −3. Although Table 3 lists $H_2O_{2,ad}^-$ as an example that carries $\gamma = -3$, this species necessarily corresponds to $\alpha = 1$ (diatomic oxygen) and $\omega = 2$ (two protons). Therefore, no physically plausible reactant set satisfies $\alpha = 1/2$ and $\omega = 0$ simultaneously, and Case III can be ruled out.

It should be noted that, in microkinetic modeling, product species do not affect the reaction rate of the RDS. This is because the elementary steps following the RDS can be reasonably assumed to be in a quasi-equilibrium state. By using the equilibrium constants for these steps, the activities of intermediate/product species can be expressed in terms of the activities of well-defined reactant species. Consequently, the derived pO_2 and pH_2O dependences in the global rate expression are determined solely by the reactants participating in the RDS, yielding mathematically identical pO_2 and pH_2O dependences.

Supplementary Note 4: Derivation of RDS for BCFZY and PBSCF at 600 °C

The pO_2 and pH_2O dependencies of point defects for PBSCF and BCFZY at 600 °C were measured and calculated. The results are presented below.

For PBSCF, at 600 °C

$$[h^{\bullet}] \propto {pO_2}^{0.078} \cdot pH_2O^0 \quad \text{(S10-1)}$$

$$[V_O^{\bullet\bullet}] \propto {pO_2}^{-0.345} \cdot pH_2O^0 \quad \text{(S10-2)}$$

$$[OH_O^{\bullet}] \propto {pO_2}^{-0.172} \cdot pH_2O^{0.5} \quad \text{(S10-3)}$$

For BCFZY, at 600 °C

$$[h^{\bullet}] \propto {pO_2}^{0.246} \cdot pH_2O^{-0.001} \quad \text{(S11-1)}$$

$$[V_O^{\bullet\bullet}] \propto {pO_2}^{-0.008} \cdot pH_2O^{-0.002} \quad \text{(S11-2)}$$

$$[OH_O^{\bullet}] \propto {pO_2}^{-0.004} \cdot pH_2O^{0.499} \quad \text{(S11-3)}$$

Following the same experimental protocol employed at 550 °C, electrochemical impedance spectroscopy measurements were conducted at the full-cell scale under systematically varied oxygen and water partial pressures (Fig. S5). From these measurements, the resistance components were extracted (Fig. S6), and the partial pressure dependencies of R1 (Fig. S7), identified as the RDS, were subsequently derived.

Consequently, as summarized in Table S2 and Table S3, the analysis confirms that for both PBSCF and BCFZY, the RDS at 600 °C remains consistent with the reaction mechanism observed at 550 °C.

Supplementary Note 5: Dependence of point defects on oxygen and water partial pressures

As expressed in Eq. S7, the total electrical conductivity is proportional solely to the hole concentration, as the ionic contribution is negligible. Equilibrium conductivity values were obtained from the data presented in Fig. 3b ($p$$H_2O$ variation at 550 °C) and Fig. S2b ($p$$O_2$ variation at 550 °C). By analyzing the power-law relationships using log-log plots of conductivity versus $p$$O_2$ and $p$$H_2O$, the corresponding exponents were determined and established as the dependencies of the hole concentration on $p$$O_2$ and $p$$H_2O$ (Eq. 5-1).

$$K_O = \frac{\left[O_o^x\right][h^\bullet]^2}{p_{O_2}^{1/2}[V_o^{\bullet\bullet}]} \tag{S12}$$

$$K_w = \frac{[OH_o^\bullet]^2}{p_{H_2O}\left[V_o^{\bullet\bullet}\right][O_o^x]} \tag{S13}$$

Subsequently, by substituting the derived $p$$O_2$ and $p$$H_2O$ dependencies of the hole concentration into the equilibrium relationships (Eq. S12) described by Eq. 3-1, the partial pressure dependencies of the oxygen vacancy concentration ($[V_O^{\bullet\bullet}]$) were determined. Finally, the partial pressure dependence of the proton concentration ($[OH_O^\bullet]$) was derived by substituting the determined oxygen vacancy dependence into Eq. S13.

Supplementary Note 6: Theoretical framework for RDS analysis under overpotential conditions

Based on the theoretical framework proposed by Z. Guan et al.,[3] the applicability of the current methodology extends to conditions under applied bias. The following discussion clarifies the validity of this analysis under overpotential before addressing the behavior of the Rate-Determining Step (RDS).

In describing the electrochemical reaction, the chemical potential of the gas-phase oxygen is defined as μ_{O_2} ,while the chemical potential of the defect species participating in the reaction within the cathode as μ_{def} (equivalent to μ_{ODE} in the reference). At open-circuit voltage (OCV), the system is at equilibrium, where the chemical potential of oxygen gas equals that of the defect species participating in the reaction.

$$\mu_{O_2} = \mu_{def} = \mu_{O_2}^{\circ} + k_B T \cdot lnpO_2 \tag{S14}$$

This framework assumes a surface-reaction-limited model, where the ionic gradient within the cathode and the ohmic drop are assumed to be negligible. Consequently, the ionic electrochemical potential is considered to remain constant and does not shift significantly when an overpotential is applied. When an overpotential (η) is applied to the electrode, it primarily shifts the electrochemical potential of the electrons($\tilde{\mu}_e$) from its equilibrium state. According to the fundamental relation of electrochemistry, this change in electron potential is expressed as:

$$\Delta\tilde{\mu}_e = -e\eta \tag{S15}$$

In a surface-reaction-limited system, this shift in electron energy serves as the primary driving force for the reaction. The chemical potential of the defect species participating in the reaction, $\Delta\mu_{def}$, is directly coupled to the electrochemical potential of the electrons.

$$\Delta\mu_{def} = -4\Delta\tilde{\mu}_e = 4e\eta \tag{S16}$$

where 4e represents the number of electrons involved in the reaction of one oxygen molecule. This equation demonstrates that the applied overpotential is equivalent to a change in the thermodynamic state of the defect species participating in the reaction, providing the necessary driving force to shift the system from equilibrium.

Based on the Nernst-like relationship, the shift in the chemical potential of the defect species participating in the reaction ($\Delta\mu_{def} = -4\Delta\tilde{\mu}_e$) can be reformulated to define an effective thermodynamic state. By substituting the overpotential term (4eη) into the chemical potential expression for oxygen gas, we define the electrode oxygen fugacity ($pO_{2,eff}$)

$$\mu_{def} + 4e\eta = \mu_{O_2}^{\circ} + k_B T \cdot lnpO_2 + 4e\eta = \mu_{O_2}^{\circ} + k_B T \cdot lnpO_{2,eff} \tag{S17}$$

$$pO_{2,eff} = pO_2 exp(\frac{4e\eta}{k_B T}) \quad \text{(S18)}$$

Thermodynamically, this means that applying an overpotential is equivalent to changing the "virtual" oxygen pressure that the defect species participating in the reaction perceive. Under bias, the electrode behaves as if it were in equilibrium with $pO_{2,eff}$ rather than the external pO_2.

Furthermore, the reaction rate (current density, j) far from equilibrium can be expressed as a function of both the external partial pressure and this internal fugacity ($pO_{2,eff}$):

$$J \propto pO_2^{1/n} \cdot pO_{2,eff}^{\lambda} \quad \text{(S19)}$$

Where $1/n$ and λ represent the reaction orders associated with the gas-phase species and the solid-state defects, respectively.

Moreover, when the overpotential (η) is held constant, the electrode oxygen fugacity ($pO_{2,eff}$) once again becomes a direct function of the external oxygen partial pressure (pO_2). This means that the reaction rate (j) can be expressed as a function of pO_2 under a fixed bias, just as we did for the RDS analysis under OCV conditions.

While the fundamental proof of this fugacity model was originally established for Solid Oxide (SO) systems, we believe this framework is fully extensible to Protonic Ceramic (PC) systems by incorporating the hydration equilibrium. In PC systems, not only the effective oxygen fugacity but also the effective water vapor pressure ($pH_2O_{,eff}$) can be determined as a function of the applied bias.

However, a crucial point of caution is that, under an applied bias, the effective partial pressures perceived by defect species can deviate substantially from the externally imposed gas-phase conditions. In particular, when a cathodic overpotential is applied in the fuel-cell operating direction, the effective oxygen partial pressure experienced by the cathode is expected to decrease significantly relative to the external oxygen partial pressure, while the effective water vapor pressure is conversely anticipated to increase.

This shift provides the conceptual basis for extending the present methodology to biased operation. If the transport properties of the electrolyte in a protonic ceramic cell are known, and If we possess a comprehensive defect map (i.e., defect concentration data over a sufficiently wide range of pO_2 and pH_2O), the pressure dependence of reaction resistances measured under bias can be interpreted in terms of the corresponding intrinsic defect chemistry. Under such conditions, the rate-determining step under actual operating bias can, in principle, be identified using the same analytical framework employed under OCV conditions.

However, evaluating Protonic Ceramic Cells under overpotential conditions still presents several challenges. A primary issue is that hole conduction can occur within the electrolyte; consequently, it is difficult to predict how this hole conduction in the electrolyte affects the air

electrode evaluation under overpotential conditions. Specifically, in Electrolysis (EC) mode, According to Duan et al.,[4] the low Faradaic efficiency in Protonic Ceramic Electrolysis Cells (PCECs) is primarily attributed to electronic leakage caused by minority p-type electronic conduction (hole conduction). In electrolysis mode, the electrochemical potential throughout the electrolyte membrane is predominantly governed by the oxidizing conditions of the positive electrode. Especially at higher current densities, this electronic transport number further increases due to the elevated local oxygen partial pressure and decreased steam concentration at the positive electrode interface, leading to intensified electronic shorting.

Moreover, Sumi et al.[5] demonstrated that current leakage significantly distorts electrochemical diagnostics in both modes; in electrolysis, it manifests as inductive loops and deceptive ohmic reductions that mask true transport properties. Conversely, in fuel cell mode, leakage offsets the external current, causing polarization resistances to anomalously increase or peak due to the minimization of net ionic current. These distortions obscure intrinsic electrode kinetics, complicating the identification of rate-determining steps. Consequently, the hole conductivity leads to underestimated efficiencies and prevents accurate prediction of cell behavior under overpotential conditions.

Second, the local consumption of oxygen and the simultaneous generation of water at the electrode surface during FC mode operation introduce significant uncertainties that can undermine the accuracy of the analysis. Specifically, the electrochemical reaction in FC mode leads to a continuous depletion of oxygen and an accumulation of water vapor at the reaction sites. This phenomenon creates a substantial discrepancy between the precisely controlled bulk gas-phase concentrations and the actual local partial pressures $pO_{2,\,local}$ and pH_2O_{local} at the electrode/gas interface.

Nevertheless, previous studies—in particular that of Y Okuyama et al.[6]—have demonstrated that the combined use of isotope effects and current-dependence analysis offers a useful framework for disentangling complex impedance responses under overpotential conditions. By systematically correlating isotope-sensitive impedance components with their current dependence, Y Okuyama et al. successfully distinguished flux-dependent charge or ion transfer reactions from quasi-equilibrium surface processes and assigned individual resistance contributions to fuel-electrode reactions, air-electrode processes, and steam formation. These findings underscore the importance of complementary diagnostic strategies for achieving a more reliable and physically meaningful interpretation of electrochemical behavior in protonic ceramic cells under practical operating conditions.

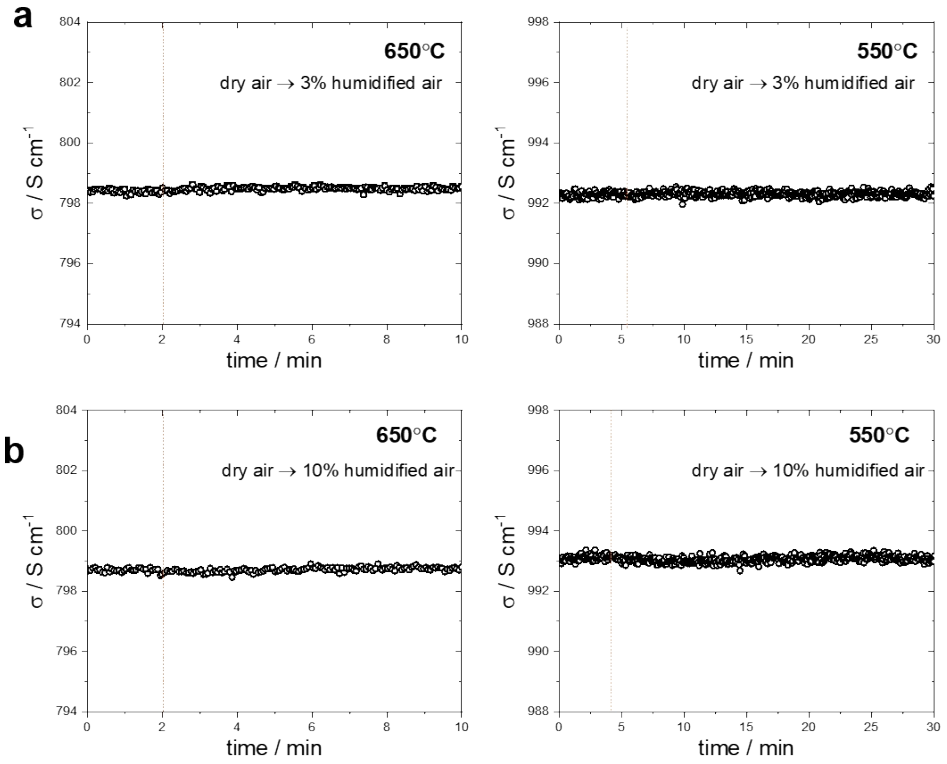

Fig. S1. Conductivity responses of PBSCF measured at 550 °C and 650 °C upon switching from dry to humidified atmospheres. Panels (a) correspond to a transition to 3% H_2O-humidified air, while panels (b) correspond to a transition to 10% H_2O-humidified air.

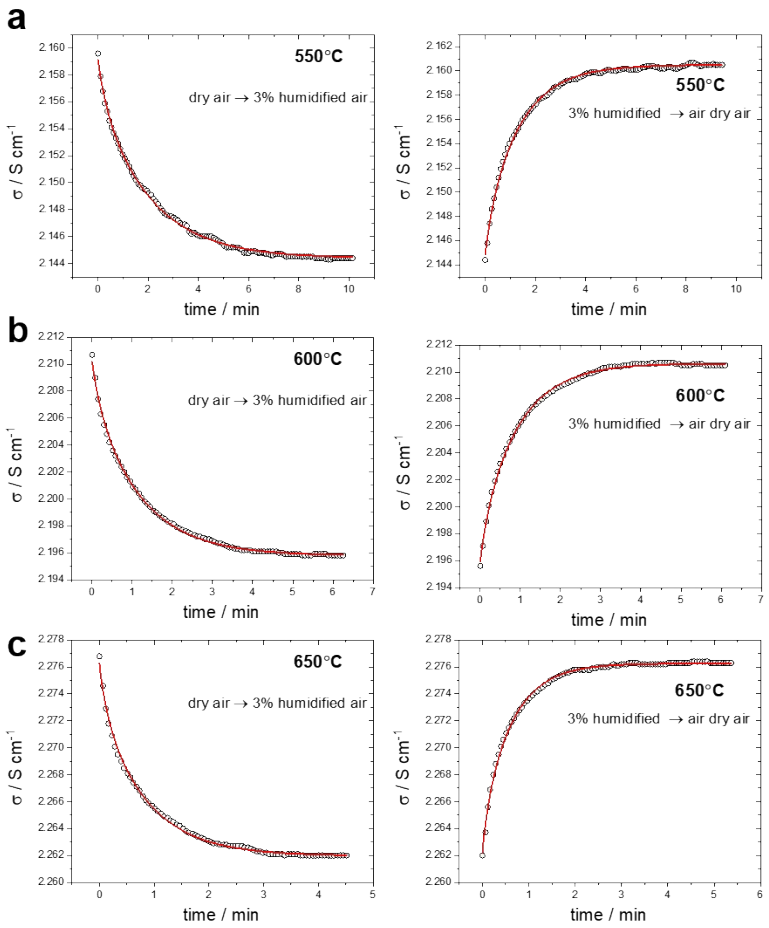

Fig. S2. Electrical conductivity relaxation (ECR) profiles of BCFZY upon gas switching between dry and 3% humidified conditions (pO_2 = 0.156 atm), showing both forward (dry → wet) and reverse (wet → dry) responses at (a) 550 °C, (b) 600 °C, and (c) 650 °C. The experimental data (symbols) were fitted (red lines) to extract the chemical diffusion coefficient (D_{chem}) and surface reaction rate constant (k_{chem}) associated with the hydrogenation process.

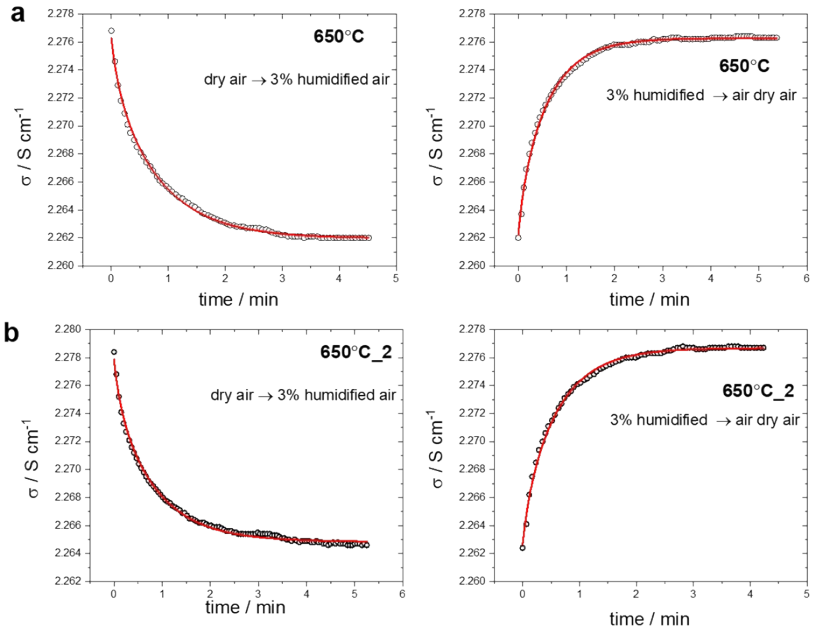

Fig. S3. ECR profiles of BCFZY at 650 °C during hydrogenation, together with fitted curves obtained from two independent measurements.

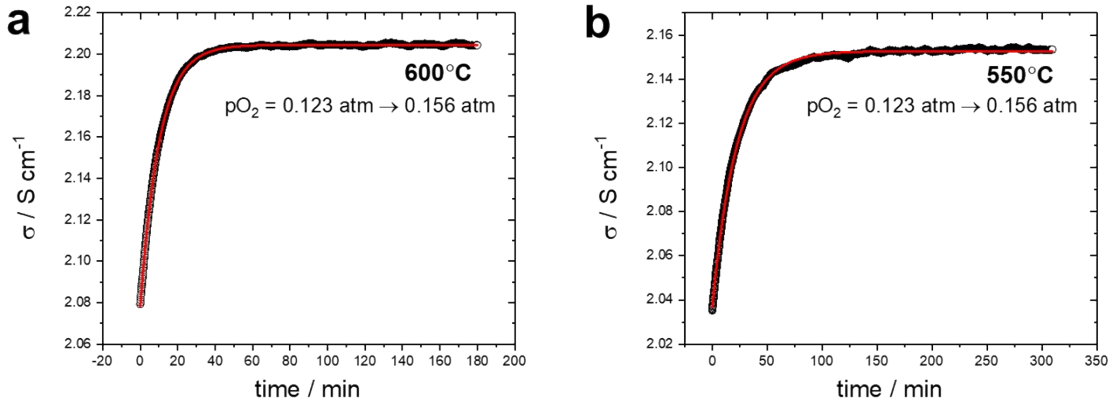

Fig. S4. ECR profiles of BCFZY upon a step increase in oxygen partial pressure from 12.3% to 15.6% pO_2 at (a) 600 °C (b) 550 °C. The red lines represent NLLS fits of experimental data, performed to extract D_{chem} and k_{chem} for the oxygen reduction reaction (ORR).

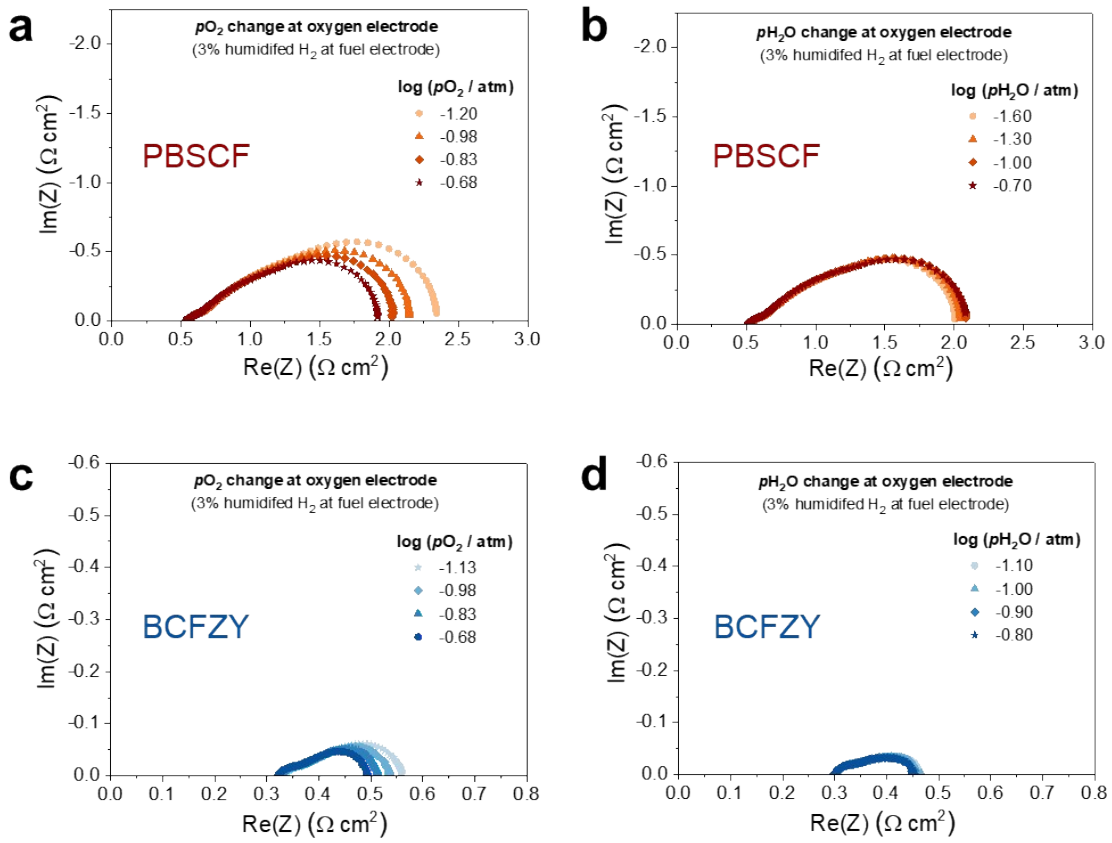

Fig. S5. Electrochemical impedance spectra (Nyquist plots) of PCFCs with PBSCF and BCFZY cathodes measured at 600 °C under different gas conditions. (a, b) Effects of varying pO_2 and pH_2O at the cathode for the PBSCF cathode, respectively; (c, d) corresponding effects of pO_2 and pH_2O variation at the cathode for the BCFZY cathode.

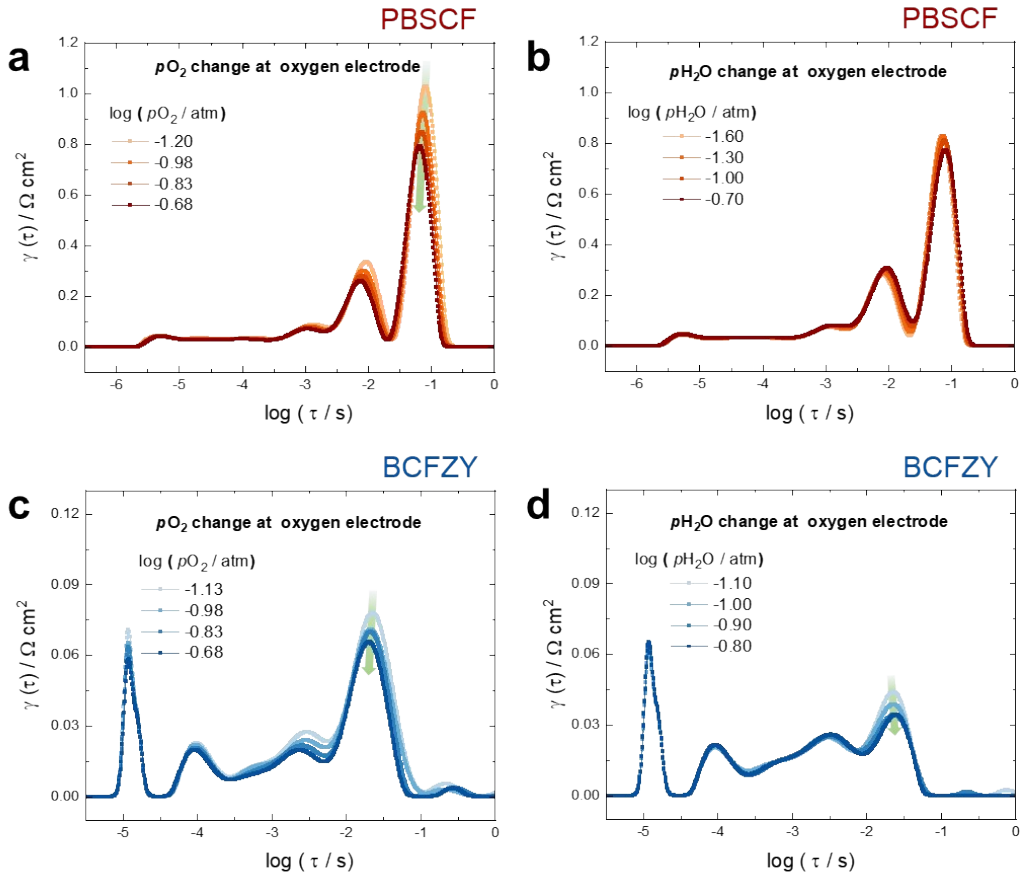

Fig. S6. Distribution of relaxation time (DRT) spectra of PCFCs with PBSCF and BCFZY cathodes measured at 600 °C under various gas conditions. (a, b) Effects of varying pO_2 and pH_2O at the cathode for the PBSCF cathode, respectively; (c, d) corresponding effects of pO_2 and pH_2O variation at the cathode for the BCFZY cathode.

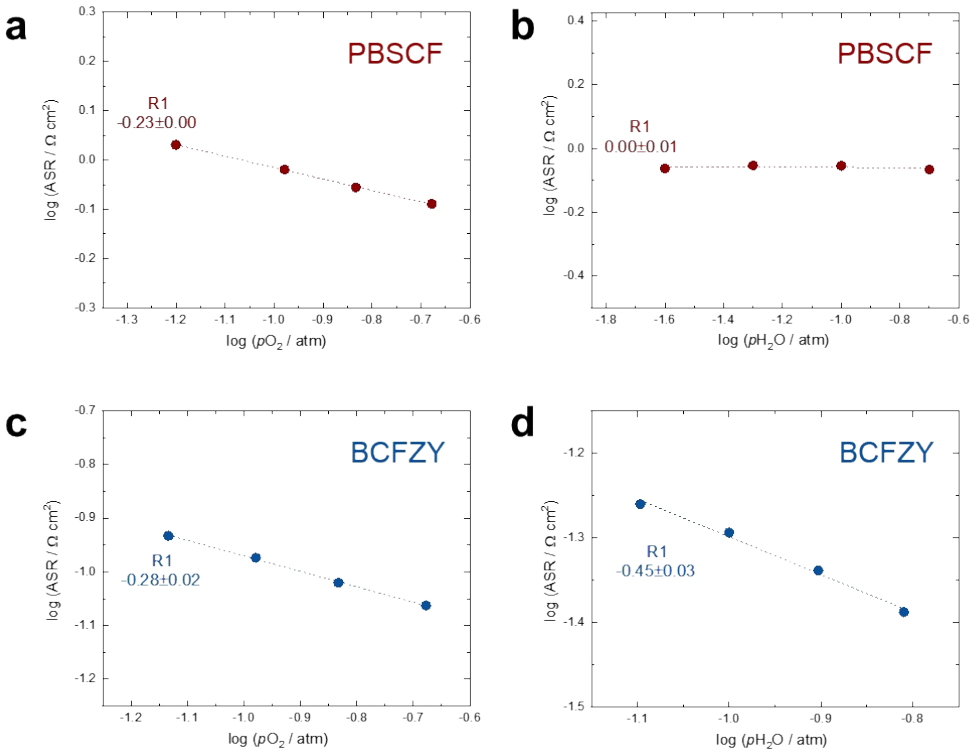

Fig. S7. Dependence of the area-specific polarization resistance (ASR) for the R1 component (RDS) on partial pressures at 600 °C. (a, b) pO_2 and pH_2O dependencies of R1 for the PBSCF cathode; (c, d) corresponding dependencies for the BCFZY cathode.

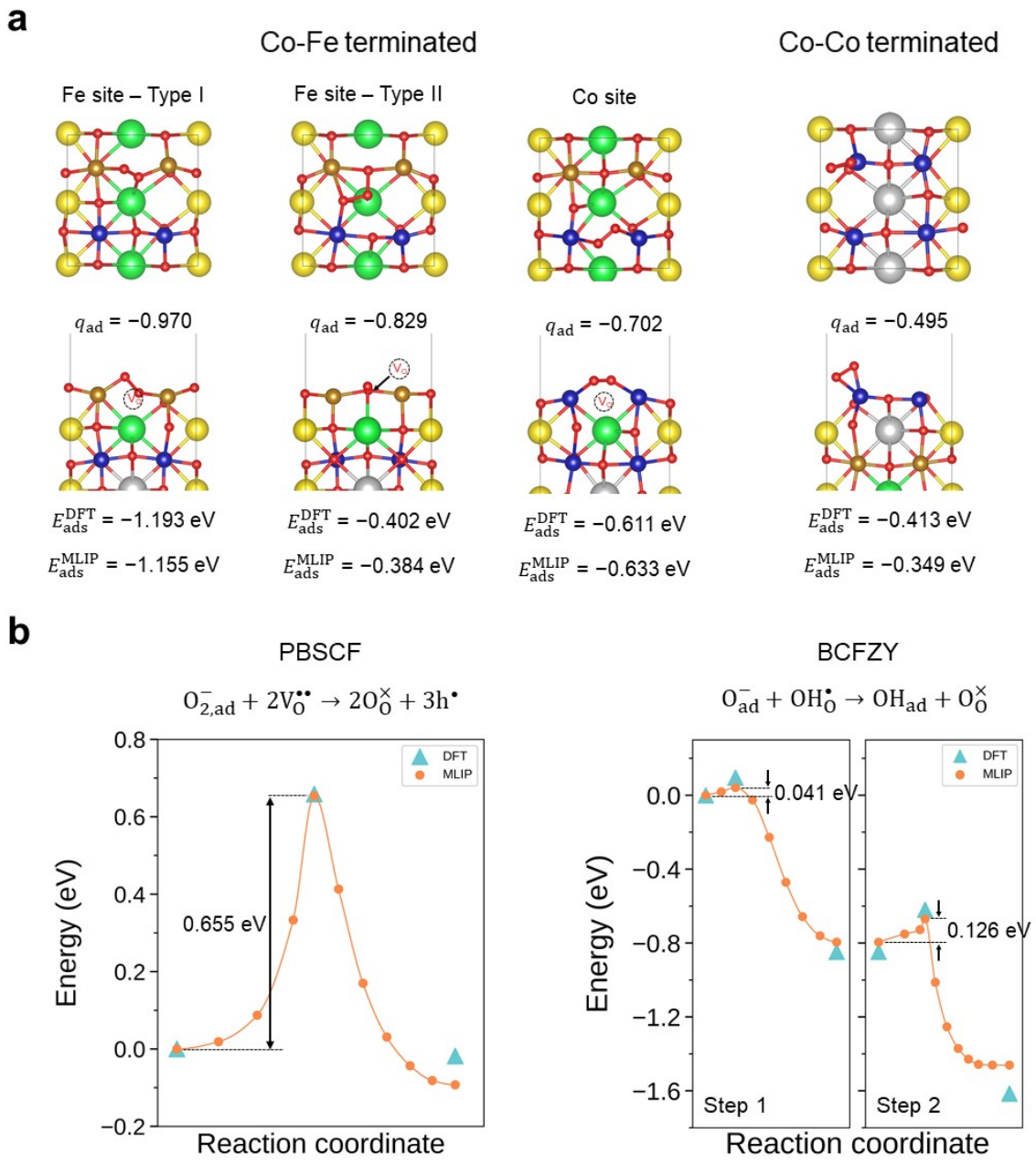

Fig. S8. Atomic structures of the defective (a) and molecule adsorbed surface (b). The dashed line circles indicates the oxygen vacancies, and ΔG_{vac} is Gibbs free energy for vacancy formation. The atomic charges of adsorbed oxygen molecule are denoted by q_{ad}, and the adsorption energy is presented by E_{ads}. The E_{ads}^{DFT} and E_{ads}^{MLIP} denote the adsorption energies computed by DFT and MLIP, respectively. These results demonstrate that the DFT and MLIP show comparable results for adsorption energy.

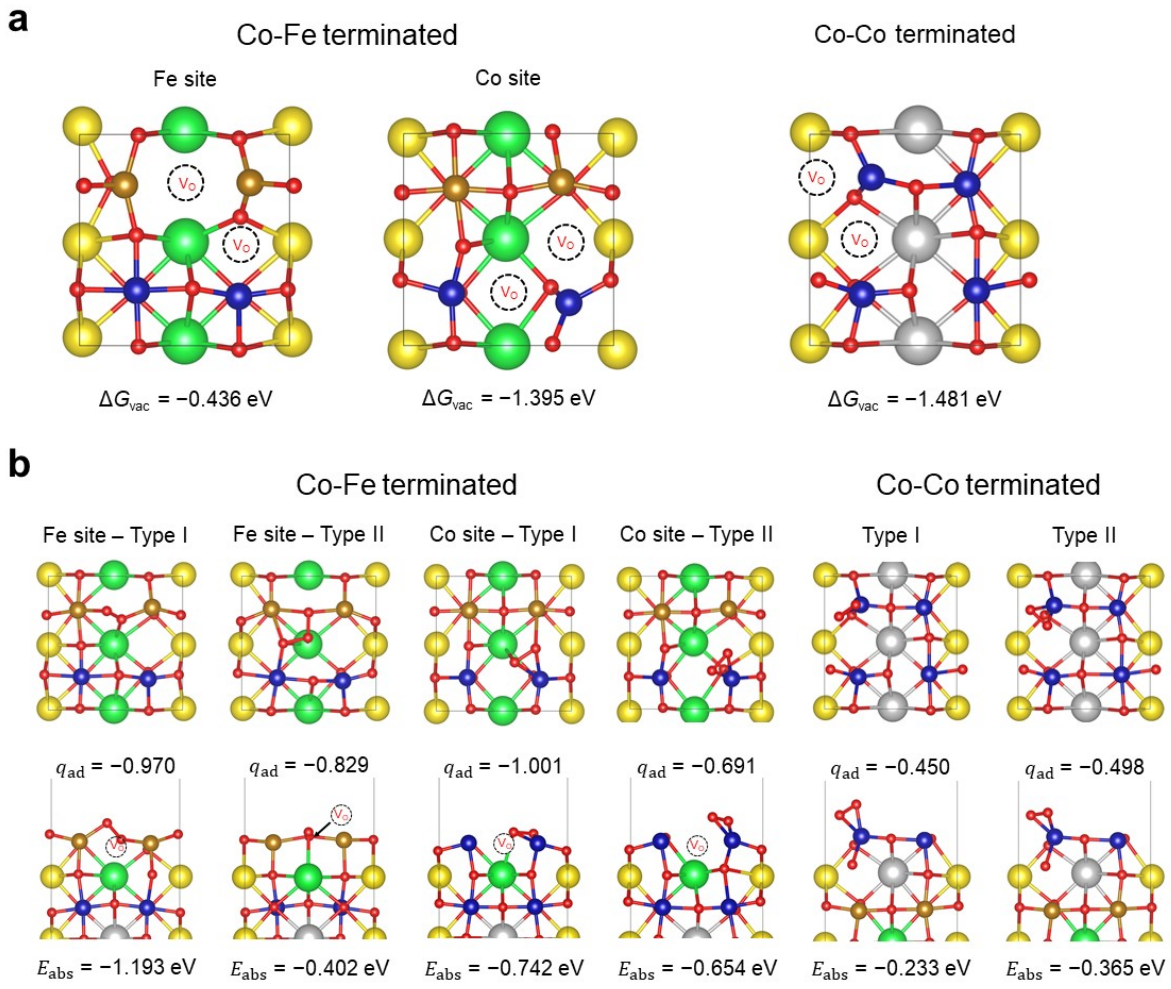

Fig. S9. (a) Double vacancy and (b) O2 adsorption geometries which was considered in this study.

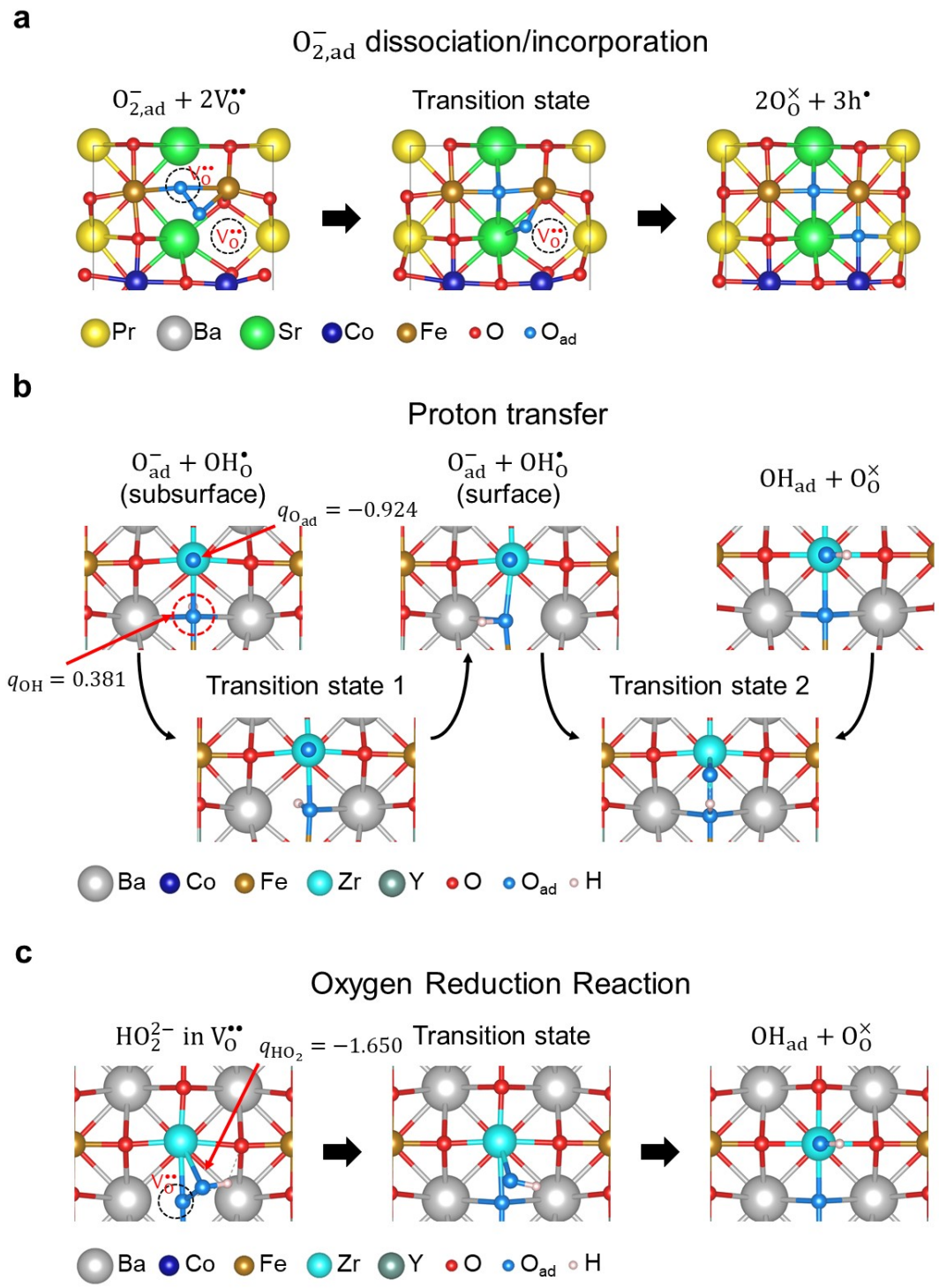

Fig. S10. Top-view of the initial, transition-state, and final structures of reactions studied in this work.

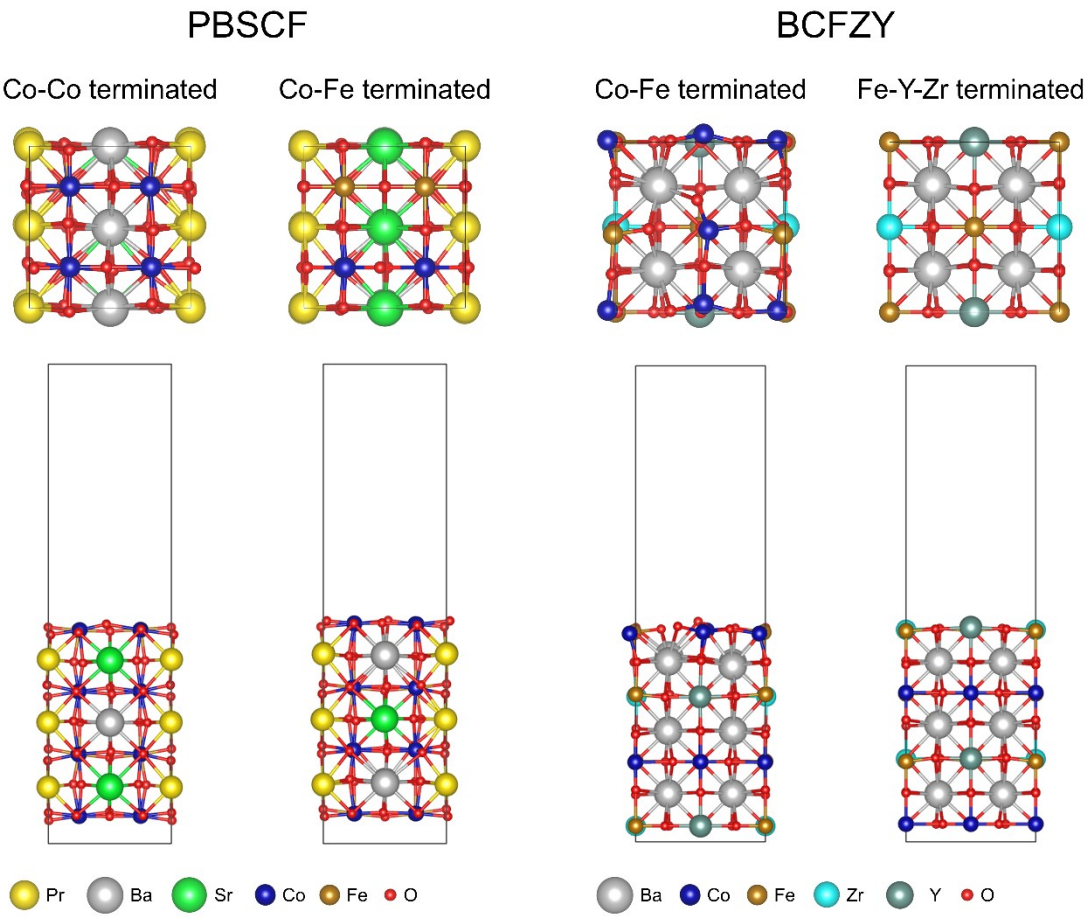

Fig. S11. Slab structures of the PBSCF and BCFYZ. The slab structures were constructed by low-index planes of PBSCF and BCFZY bulk structures, which are the (100) and (001) planes. The vacuum space of each slab was set to 15 Å.

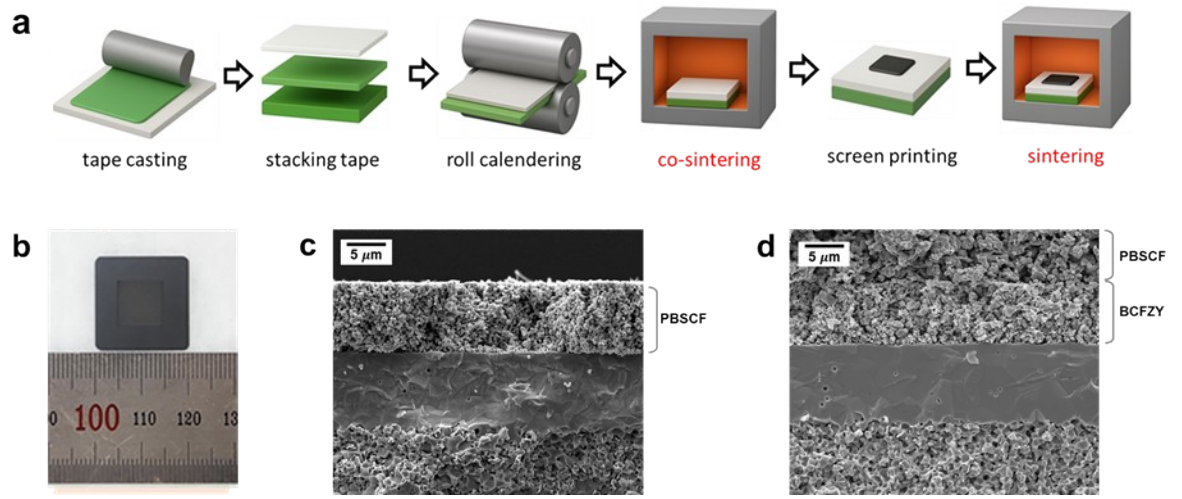

Fig. S12. Fabrication procedure, photograph, and cross-sectional microstructures of 2 × 2 cm² PCFC single cells with PBSCF and BCFZY cathodes. (a) Schematic illustration of the tape-based fabrication process, including tape casting, stacking, roll calendaring, co-sintering, screen printing, and final sintering. (b) Photograph of the fabricated single cell (2 × 2 cm²). (c, d) Cross-sectional SEM images of the cells employing PBSCF and BCFZY cathodes, respectively, both using BCZYYb electrolytes.

Table S1. Combination of stoichiometric coefficients, which satisfied total number of oxygen vacancies = 0 or 2. In the case that the cathode material follows a dehydrogenation mechanism, the total number of oxygen vacancies involved in the overall process is zero, corresponding to Case 1. In the cases that the cathode follows a dehydration mechanism, the total number of oxygen vacancies involved is two, corresponding to Cases 2-7. For this latter scenario, we classified all possible allocations of the two oxygen vacancies among the stages before the RDS, during the RDS, and after the RDS into Cases 2-7. Importantly, the exponent (β) in $[V_O^{\bullet\bullet}]^{\beta}$ exactly matches the number of $V_O^{\bullet\bullet}$ during RDS.

Cases.	# of $V_O^{\bullet\bullet}$ before RDS	# of $V_O^{\bullet\bullet}$ during RDS	# of $V_O^{\bullet\bullet}$ after RDS	Total # of $V_O^{\bullet\bullet}$ participating in ORR	Exponent in $[V_O^{\bullet\bullet}]$
1	0	0	0	0	0
2	2	0	0	2	0
3	1	1	0	2	1
4	1	0	1	2	0
5	0	2	0	2	2
6	0	1	1	2	1
7	0	0	2	2	0

R1 in PBSCF	$\vec{R} \propto {pO_2}^{\alpha}[V_O^{\bullet\bullet}]^{\beta}[h^{\bullet}]^{\gamma}[OH_O^{\bullet}]^{\omega}$				$\vec{R} \propto {pO_2}^{A} \cdot {pH_2O}^{B}$		Possible reaction expressions
	α	β	γ	ω	A	B	
Case I	1	2	-1	0	0.232	0	$O_{2,ad}^{-} + 2V_O^{\bullet\bullet} \rightarrow 2O_o^{\times} + 3h^{\bullet}$ $(O_2^{-} in V_O^{\bullet\bullet}) + V_O^{\bullet\bullet} \rightarrow 2O_o^{\times} + 3h^{\bullet}$
Case II	1	2	0	0	0.310	0	$O_{2,ad} + 2V_O^{\bullet\bullet} \rightarrow 2O_o^{\times} + 4h^{\bullet}$ $(O_2 in V_O^{\bullet\bullet}) + V_O^{\bullet\bullet} \rightarrow 2O_o^{\times} + 4h^{\bullet}$
Experimental result	n/a				0.23±0.004	0.00±0.001	-

Table S2. Analysis of possible R1 cases (Cases I and II) at 600 °C in PBSCF.

Table S3. Analysis of possible R1 cases at 600 °C in BCFZY

R1 in BCFZY	$\vec{R} \propto {pO_2}^{\alpha}[V_O^{\bullet\bullet}]^{\beta}[h^{\bullet}]^{\gamma}[OH_O^{\bullet}]^{\omega}$				${pO_2}^{A} \cdot {pH_2O}^{B}$		Possible reaction expressions
	α	β	γ	ω	A	B	
Case I	1/2	0	-1	1	0.250	0.500	$O_{ad}^{-} + OH_O^{\bullet} \rightarrow OH_{ad} + O_o^{\times}$
Case II	1/2	1	-1	1	0.242	0.498	No valid reaction step
Case III	1	1	-3	1	0.250	0.500	$(HO_2^{2-} in V_O^{\bullet\bullet}) \rightarrow OH_{ad} + O_o^{\times}$
Experimental result	n/a				0.28±0.02	0.45±0.02	-

Table S4. Fitted kinetic parameters (k_{chem} and D_{chem}) and residuals obtained from ECR analyses of the hydrogenation reaction in BCFZY at 650, 600, and 550 °C for both dry → wet and wet → dry transitions.

Temperature (°C)	condition	k_{chem} (cm s^{-1})	D_{chem} (cm^2 s^{-1})	Residual
650	Dry → Wet	$(2.46 \pm 0.03) \times 10^{-3}$	$(7.48 \pm 0.10) \times 10^{-6}$	0.9977
	Wet → Dry	$(1.85 \pm 0.02) \times 10^{-3}$	$(1.15 \pm 0.01) \times 10^{-5}$	0.9975
600	Dry → Wet	$(1.16 \pm 0.01) \times 10^{-3}$	$(5.82 \pm 0.06) \times 10^{-6}$	0.9983
	Wet → Dry	$(1.09 \pm 0.01) \times 10^{-3}$	$(8.23 \pm 0.08) \times 10^{-6}$	0.9980
550	Dry → Wet	$(7.50 \pm 0.05) \times 10^{-4}$	$(3.25 \pm 0.02) \times 10^{-6}$	0.9977
	Wet → Dry	$(7.53 \pm 0.06) \times 10^{-4}$	$(5.58 \pm 0.04) \times 10^{-6}$	0.9975

Table S5. Fitted kinetic parameters (k_{chem}, D_{chem}) and residuals from ECR fitting of the hydrogenation reaction in BCFZY at 650 °C for two independent trials.

Trial.	condition	k_{chem} (cm s^{-1})	D_{chem} (cm^2 s^{-1})	Residual
1	Dry → Wet	$(2.46 \pm 0.03) \times 10^{-3}$	$(7.48 \pm 0.10) \times 10^{-6}$	0.9977
	Wet → Dry	$(1.85 \pm 0.02) \times 10^{-3}$	$(1.15 \pm 0.01) \times 10^{-5}$	0.9975
2	Dry → Wet	$(2.72 \pm 0.04) \times 10^{-3}$	$(7.15 \pm 0.10) \times 10^{-6}$	0.9954
	Wet → Dry	$(1.96 \pm 0.03) \times 10^{-3}$	$(1.15 \pm 0.02) \times 10^{-5}$	0.9967

References

1. Y. Shin, M. D. Sanders, E. Truong, S. Majumder, B. Cladek, M. Walker, B. Ogbolu, R. Zhang, G. A. Evmenenko and Y.-Y. Hu, *Solid State Ionics*, 2025, **429**, 116962.
2. D. Poetzsch, R. Merkle and J. Maier, *Faraday Discussions*, 2015, **182**, 129.
3. Z. Guan, D. Chen and W. C. Chueh, *Physical Chemistry Chemical Physics*, 2017, **19**, 23414-23424.
4. C. Duan, R. Kee, H. Zhu, N. Sullivan, L. Zhu, L. Bian, D. Jennings and R. O'Hayre, *Nature Energy*, 2019, **4**, 230-240.
5. H. Sumi, H. Shimada, K. Watanabe, Y. Yamaguchi, K. Nomura, Y. Mizutani and Y. Okuyama, *ACS Applied Energy Materials*, 2023, **6**, 1853-1861.
6. Y. Okuyama, K. Kasuga, M. Shimomura, Y. Mikami, K. Yamauchi, T. Kuroha and H. Sumi, *Journal of Power Sources*, 2023, **586**, 233647.